Journal of the Korean Electrochemical Society
Vol. 6, No. 4, 2003, 271-281

총 설

Pitting Corrosion of Inconel Alloy 600 at Elevated Solution Temperatures

Jin-Ju Park and Su-Il Pyun†

Department of Materials Science and Engineering, Korea Advanced Institute of Science and Technology, 373-1, Guseong-dong, Yuseong-gu, Daejeon, 305-701, Republic of Korea

(Received June 23, 2003 : Accepted August 11, 2003)

Abstract : The present article is concerned with pitting corrosion of Inconel alloy 600 at elevated solution temperatures. This article first summarized the previous works on the characteristics and the growth models of oxide film grown on alloy 600 at elevated solution temperatures. Thereafter, this article reviewed previous works on the morphological study on pitting corrosion of alloy 600 as functions of solution temperature and such anion additives as thiosulphate, sulphate, nitrate and bicarbonate ions in terms of pit morphology and its fractal dimension.

Key words: Pitting corrosion, Alloy 600, Elevated solution temperature, Oxide film, Pit morphology, Fractal dimension

1. Introduction

Inconel alloy 600 is a Ni-based alloy widely used as a steam generator tubing material in pressurized water reactors nuclear power plants. In this application, tube failures caused by pitting corrosion have been reported[1-5]. Therefore, a study on pitting corrosion of alloy 600 is of great interest in both the industrial application and theoretical viewpoint.

Pitting behaviour is mainly dependent on such environment factors as solution temperature[6,7] and composition of the electrolyte[8,9]. In this respect, the effects of solution temperature and anion additives on pitting corrosion have been studied extensively in view of changes in pitting potential and current density[10,11].

It is generally recognized that the formation and growth of the corrosion pits are strongly related to the characteristics of oxide film formed on the metal surface, particularly in the case of pitting corrosion at elevated solution temperature. Therefore, the observed changes in pitting behaviour of alloy 600 at elevated solution temperature have been often related to changes in the composition, structure and properties of the passive oxide film with respect to solution temperature.

In this respect, this paper first discussed the properties and the growth models of oxide film grown on Inconel alloy 600 at elevated solution temperatures. Thereafter, this article reviewed the morphological change of the corrosion pits formed on alloy 600 as functions of solution temperatures and such anion additives as thiosulphate, sulphate, nitrate and bicarbonate ions in terms of pit morphology and its fractal dimension.

2. Properties and growth models of oxide film formed on alloy 600 at elevated solution temperature

2.1. Chemical composition and structure of oxide film grown at elevated solution temperature

Single-layer or double-layer oxide films are formed on alloy 600 during exposure to elevated temperature water. Surface analysis methods with high resolution and sensitivity must be applied to examine the structure and composition of such oxide layers. The general features of the oxide structure were described with special emphasis on the publications of D. Lister and co-workers who studied morphology of such oxide layers extensively[12-15]. Their results were representative for the picture which can be gained from the literature[14-16].

The most striking characteristic of experimental impedance spectra was the appearance of two peaks in the phase angle at temperatures above 100°C. It could be related to the well-known duplex structure of passive films formed on Ni-Fe-Cr alloys in elevated temperature solution. The outer, crystalline, part of oxide film was reported to be Fe-rich, while the inner, amorphous, protective layer was Cr-rich.

The double-layer oxide film usually found on Ni-Fe-Cr alloys after exposure to water at temperatures above 150°C is shown schematically in Fig. 1. Morphology of oxide film is

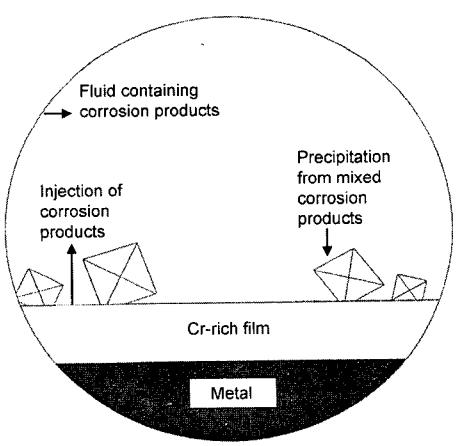

Fig. 1. Schematic picture of the two-layer structure oxide film on Ni-Fe-Cr alloy at elevated temperature water[15].

†E-mail: sipyun@webmail.kaist.ac.kr

similar to the typical duplex structure found in iron and iron-based alloys corroded in high temperature aqueous media[17,18]. The film consists of a uniform inner layer that grows into the metal and the outer layer formed by a regular deposit of octahedral crystal. Fig. 2 shows typical SEM micrograph of morphology of the inner layer after partial dissolution of the outer layer at 300°C. It was observed that the octahedral crystalline outer layer was formed on the inner oxide layer as illustrated in Fig. 1. The density of crystals is influenced by surface finish, chemistry of the solution and time of exposure[14,15].

The inner layer consists of a Cr-rich spinel oxide layer. The thickness of the inner layer is usually in the range of 50 to 100 nm[14,20]. The structure of the inner layer is described as being badly crystallized[21]. According to Lister et al.[14] the inner layer is amorphous. Amorphous inner oxide layer contains neither grain boundary and dislocations acting as easy paths for the transport of ions nor segregations that give rise to preferential corrosion. Therefore, superior corrosion resistance is attributed to amorphous passive films. The amorphous state is thermodynamically meta-stable, thus crystallization can be induced by an increase in solution temperature.

Corrosion products present in high temperature water favour the formation of the outer layer. As reported by Lister et al.[14,15], a double layer can be observed on Ni-Fe-Cr alloys after exposure to high temperature water containing corrosion products. On the other hand, exposure to water without corrosion products results in the formation of a single-layer oxide film.

It is generally assumed that both layers contain pores or other defects[19,22,23]. Pores and defects play an essential role in all models of film growth. Asakura et al.[19] ascribed the formation of these defects to increasing residual stresses in the growing film, leading to cracking. According to Stellwag[24], exposure of the initially amorphous passive film to high temperatures induces crystallization processes, thus causing defects.

In Ni-Cr-Fe alloys, from observation of SEM micrographs of oxide layer, at relatively low temperature, thin and fine crystalline oxide layers grew on the Ni-Cr-Fe alloy surface, while at higher temperature thick and coarse crystalline layers grew. Thus, the increase in the layer porosity with increasing temperature, which is connected with the change of the crystallinity, favours the ion penetration through the layer. Consequently, at higher temperatures, oxide film may be more porous and hence less protective[25].

Fig. 2. Typical SEM micrograph of morphology of the inner oxide layer after partial dissolution of the outer oxide layer grown on alloy 600 in alkalinized water at 300°C[18].

In relation to oxide film porosity, Wang et al.[22] reported that from ac impedance results, it follows that increasing solution temperature makes the film less protective. The increase of capacitance with solution temperature might be thought to indicate either the film thickness diminishes or the film porosity increases. Since film thickening at high temperature can be observed, it is concluded that the film porosity increases with solution temperature.

2.2. Models of growth of oxide layer in elevated temperature water

2.2.1. Solid state growth model[26]

Now, let us discuss the growth models of oxide layers at elevated solution temperatures. Robertson[26] derived his model from similarities of the oxide growth in high temperature steam and water. Essential features of Robertsons solid-state growth model as follows: (1) The fine-grained inner layer grows by access of water through oxide micro-pores. (2) The alloying elements of Ni-Cr-Fe alloys pass congruently into oxide film. (3) According to the diffusion rates of the metal ions in the spinel lattice, Cr moves more slowly than Ni and Fe, and Cr is thus enriched in the inner layer. (4) The outer layer grows by outward diffusion of the metal ions, especially Ni and Fe, along oxide grain boundaries. (5) The outer layer can be released to the solution, while the Cr in the spinel lattice of the inner oxide layer is always retained.

In this connection, Robertson pointed out that Cr ions retained in the inner layer also tend to reduce the rate of diffusion of their surrounding metal ions. Thus, rate control always resides in the inner layer.

2.2.2. Metal dissolution-oxide precipitation mechanism[27]

Winkler[27] attributed the formation of both layers to a metal dissolution-oxide precipitation mechanism. Metal dissolves from active sites at the base of pores. The associated increase in concentration of the dissolved metal species enables precipitation of oxides at these sites. Mixed oxides precipitate from the constituents on the pore solution in the order of their formation free energy. That is, mixed oxides with a high negative free energy of formation are formed first. This fact results in the concentration profiles of the alloying elements across the oxide layer. Therefore, this concentration gradient across the oxide layer causes outward diffusion of metal species through the oxide film. Thereafter, the dissolved metal species diffusing outward precipitate on the inner oxide layer in the form of mixed spinel, resulting in the formation of the outer, coarse-grained oxide layer.

The above description of essential reaction steps from the

viewpoint of solid-state processes and metal dissolution-oxide precipitation mechanisms shows that both the models are basically suited to explain the characteristic features of oxide film formed on Ni-Fe-Cr alloys in high temperature water.

2.2.3. Modified point defect model combined with diffusion-dissolution coupled model[28]

The point defect model suggested by Chao and Macdonald[29-31] is usually employed to investigate the growth kinetics of oxide film on metals. The point defect model considered that the transport of oxygen vacancy contributes to the oxide film growth, while the transport of metal vacancy causes the metal dissolution only. However, the modified point defect model by Pyun and Hong[32] suggested that the transport of metal vacancy contributes to both the oxide film growth and metal dissolution. Thus, the transport of metal vacancy should additionally be considered in the oxide film growth. As a result, they derived equation for the current transient as:

$$i = \frac{Fz^2}{N_V} D^*_{V_M^{z'}} K \frac{C_{V_M^{z'}}(m/f)\exp[zKL(t)] - C_{V_M^{z'}}(f/e)}{\exp[zKL(t)] - 1} \quad (1)$$

where $D^*_{V_M^{z'}}$ is electrochemical diffusivity of metal vacancy, $C_{V_M^{z'}}$ is the concentration of metal vacancy, z is charge umber of metal ion, K is constant ($K\vec{E} = F/RT$) being related to field strength ($\vec{E}$) and $L(t)$ is thickness as a function of time t.

In addition, the contribution of the transport of metal vacancy to the film growth and metal dissolution involves the following reaction at the oxide film/electrolyte interface:

$$(z+2)m + H_2O = (2/z)M_M + O_O + (z+2)e + 2H^+_{(aq)} + M^{z+}_{(aq)} \quad (2)$$

where m is the metal atom in the metal, M_M is metal cation in the film, O_O is oxygen anion in the film and $M^{z+}_{(aq)}$ is metal cation in the electrolyte. From Eq. (2), it should be noted that the steady-state current is entirely attributable to the current determined by the flux of metal dissolution.

Fig. 3 depicts potentiostatic anodic current transients on a logarithmic scale obtained just after interrupting the abrading action on alloy 600 at the applied anodic potential of 0.2 $V_{Ag/AgCl}$ in aqueous 0.1 M Na_2SO_4 solution at various solution temperatures 100° to 300°C. The current transients were observed to be composed of two stages. In the first stage, it was found that current density decreased rapidly with time and followed by the first current plateau. Thereafter, in the second stage, current density was observed to decrease slowly and then reached the second current plateau. This two-stage behaviour of the current transients indicates that two different kinds of layers are grown, i.e., the inner oxide layer and the outer oxide layer, and at the same time the growth kinetics of the two layers are kinetically distinguishable.

In this figure, a linear relation between log current i and log time t in the first stage of the current transient was not clearly observed. Park et al.[28] reported that the first stage of the current transient measured on alloy 600 follows satisfactorily Eq. (1). This means that the growth kinetics of the inner oxide layer of alloy 600 can be explained by the modified point defect model.

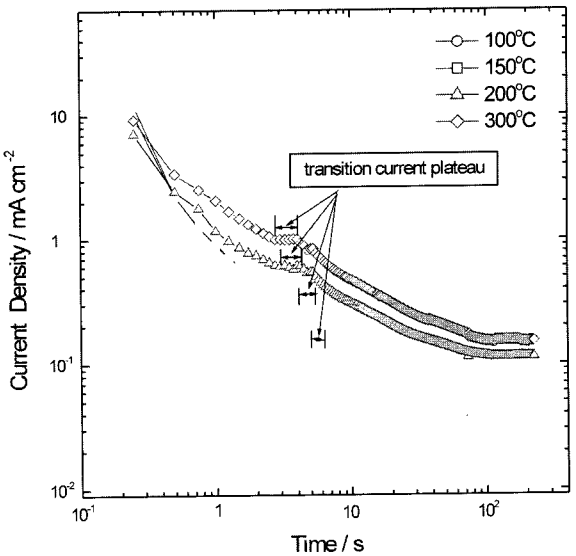

Fig. 3. Potentiostatic anodic current transients on a logarithmic scale obtained just after interrupting the abrading action on alloy 600 at the applied anodic potential of 0.2 $V_{Ag/AgCl}$ in aqueous 0.1 M Na_2SO_4 solution at 100° to 300°C.

In the case of the outer oxide layer, since the value of steady-state current level is high above 100°C, it is possible for the concentration of the dissolved metal ions passed through the inner oxide layer by diffusion to exceed the solubility limit. Thus, the metal ions are precipitated on the film surface which has been previously grown. This leads to the growth of two-layered oxide film. Consequently, the previously grown layer is called the inner layer, and successively precipitated layer is called the outer layer. As a result, they proposed a new model for the growth of the outer layer, and call it diffusion-dissolution coupled model[28].

3. Morphological change of the corrosion pits of alloy 600 as functions of solution temperature and anion additives

Now, we reviewed previous works[33-36] on the morphological change of the corrosion pits formed on alloy 600 as functions of solution temperature and anion concentration.

3.1. Effect of solution temperature

3.1.1. In thiosulphate containing chloride solution

Fig. 4 gives changes in the value of oxide film resistance R_{ox} with applied anodic potential on a semi-logarithmic scale obtained from the impedance spectra for alloy 600 in aqueous 0.1 M $Na_2S_2O_3$ + 0.1 M NaCl solution at various solution temperatures. It was noted that the value of R_{ox} decreased with increasing solution temperature over the whole applied anodic potential. This indicates that increasing

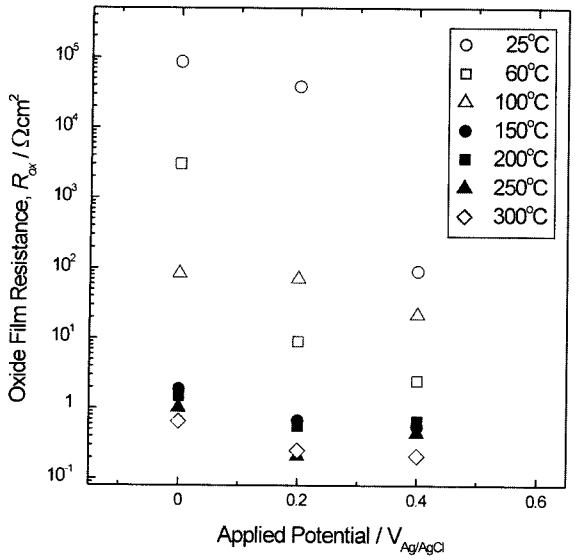

Fig. 4. Changes in the oxide film resistance R_{ox} with applied anodic potential on a semi-logarithmic scale obtained from alloy 600 in aqueous 0.1 M $Na_2S_2O_3$ + 0.1 M NaCl solution at various temperatures 25° to 300°C.

solution temperature has detrimental effect on oxide film passivity, leading to pitting corrosion[22,37,38].

Morphology of the corrosion pits formed on the specimen was examined as a function of solution temperature using SEM. Figs. 5(a) through (f) show typical SEM micrographs of pit morphology on the surface of alloy 600 subjected to a constant anodic potential of 0.8 $V_{Ag/AgCl}$ for 300 s in aqueous 0.1 M $Na_2S_2O_3$ + 0.1 M NaCl solution at 60°, 100°, 150°, 200°, 250° and 300°C, respectively. It was found that pit morphology changed from cylindrical shape made at 60°C to highly branched shape formed at 150°C[39,40] and finally it changed from highly branched shape in the early stage of the pitting process to widely grooved shape in the later stage above 200°C.

This morphological change is under the control of degree of passivity of oxide film formed on the specimen as a function of solution temperature. From the experimental result of Fig. 4, it is inferred that degree of passivity of oxide film was diminished with increasing solution temperature.

At 60°C, the pit embryos generated at such sites covered with less protective oxide film are surrounded with the region covered mainly with more protective oxide layer

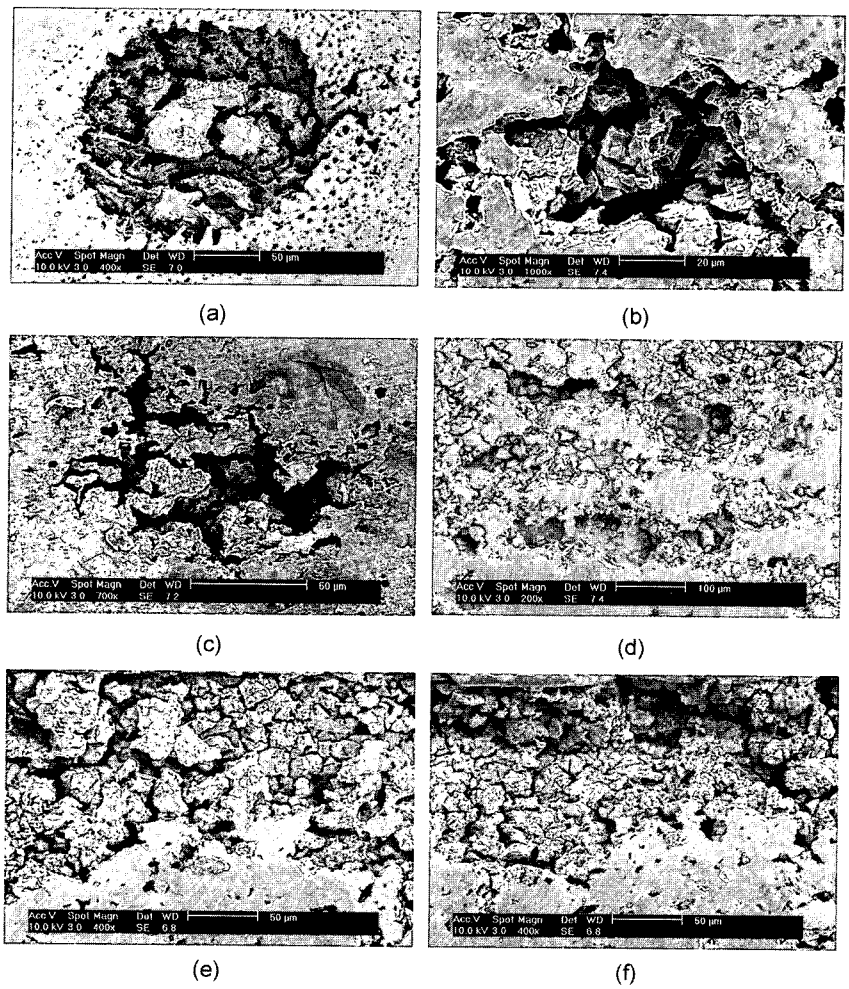

Fig. 5. Typical SEM micrographs of pit morphology on the surface of alloy 600 subjected to a constant anodic potential of 0.8 $V_{Ag/AgCl}$ for 300 s in aqueous 0.1 M $Na_2S_2O_3$ + 0.1 M NaCl solution at (a) 60°, (b) 100°, (c) 150°, (d) 200°, (e) 250° and (f) 300°C.

owing to higher degree of passivity of oxide film. Thus, the viable pit embryos have the same tendency to grow further in all radial directions and hence the grown pits finally form cylindrical shape.

In contrast, the pit embryos generated at 150°C are surrounded by the region covered predominantly with less protective oxide film due to lower degree of passivity of oxide film. The coverage by less protective oxide layer of the region immediately adjacent to the pit embryos may limit pit growth in all radial directions. Thus, the viable pit embryos have a preferred tendency to grow further in specific direction and hence the grown pits finally form highly branched shape.

Above 200°C, all the pit embryos are encircled by the region covered with non-protective oxide layer due to the lowered value of degree of oxide film passivity. Thus, they grow further in all directions, resulting in the transition in pit morphology from highly branched shape to widely grooved shape.

After SEM observation, observed pit morphology was digitized and hence pit perimeter and pit area were calculated from digitized image by using a computer program, which was developed by Shin and Go[41] in our laboratory. Thereafter, the values of the fractal dimension D_f for the various pits were determined by using perimeter-area method[42-48]. According to this method, the value of D_f of the pits is equivalent to just twice the value of the slope in the plot of pit perimeter vs. pit area on a logarithmic scale.

Fig. 6 illustrates logarithmic plots of pit perimeter vs. area for pit morphology of alloy 600 subjected to a constant anodic potential of 0.8 $V_{Ag/AgCl}$ for 300 s in aqueous 0.1 M $Na_2S_2O_3$ + 0.1 M NaCl solution as a function of solution temperature. In this figure, it was noted that the linear relationship between pit area and pit perimeter appeared. It was found that solution temperature raised the value of D_f as follows; D_f (60°C) = 1.04 ± 0.04, D_f (100°C) = 1.24 ± 0.06 and D_f (150°C) = 1.40 ± 0.1. Higher value of D_f at 150°C is due to the increase in ratio of pit perimeter to pit area, indicating the formation of the pits with highly branched shape as shown by SEM observation.

From the fractal dimension theoretically derived from fractal surface, it is accepted[42,43] that adherence to the same pit morphology is a sufficient condition for keeping constant fractal dimension of the pits during the whole pitting process. From the fractal dimension determined experimentally, it is noted that the fractal dimension of the pits maintains nearly constant in value during the whole pitting process, irrespective of pit size. Consequently, since pit size is usually proportional to time for pit growth, it can be stated that the corrosion pits has the same morphology during the whole pit growth stage at each different solution temperatures.

Fig. 7(a) presents impedance spectra in Nyquist presentation obtained from alloy 600 at the applied potential of 0.2 $V_{Ag/AgCl}$ in aqueous 0.1 M $Na_2S_2O_3$ + 0.1 M NaCl solution at various solution temperatures. In this figure, it should be stressed that the Nyquist plots were found to be depressed

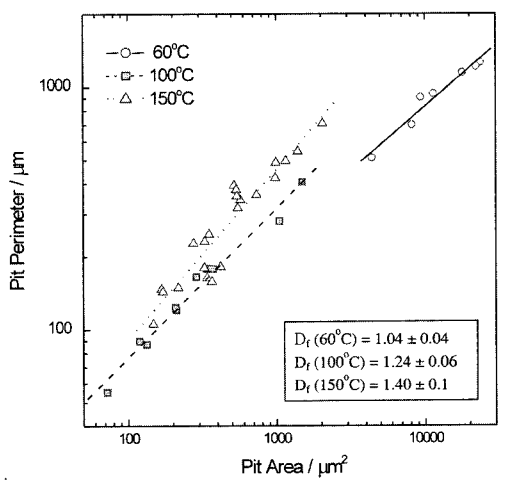

Fig. 6. Logarithmic plots of pit perimeter vs. area for pit morphology of alloy 600 subjected to a constant anodic potential of 0.8 $V_{Ag/AgCl}$ for 300s in aqueous 0.1 M $Na_2S_2O_3$ + 0.1 M NaCl solution from 60° to 150°C.

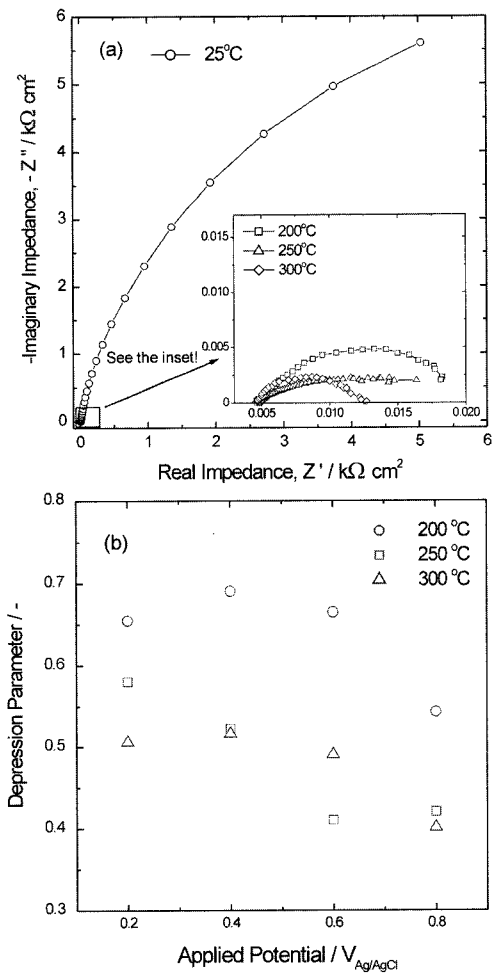

Fig. 7. (a) Impedance spectra in Nyquist presentation and (b) changes in the depression parameter with applied anodic potential obtained from alloy 600 at the applied potential of 0.2 $V_{Ag/AgCl}$ in aqueous 0.1 M $Na_2S_2O_3$ + 0.1 M NaCl solution at various solution temperatures.

more markedly from a perfect semicircle form with increasing solution temperature. This can be validated by the decrease in the depression parameter.

Fig. 7(b) demonstrates applied potential dependence of the depression parameter determined from the Nyquist plots obtained from the specimen in aqueous 0.1 M $Na_2S_2O_3$ + 0.1 M NaCl solution at various solution temperatures. The value of the depression parameter diminished with increasing solution temperature. Considering that a major cause of depression of impedance spectra is known to be of geometric origin[49-51], it is inferred that the occurrence of depression of impedance spectra of the pitted specimen stems from the increase in the surface roughness of the specimen.

3.1.2. In chloride solution

Fig. 8 gives potentiodynamic polarization curves of alloy 600 with a scan rate of 0.5 mVs^{-1} in aqueous 0.5 M NaCl solution at various solution temperatures. As solution temperature increased, it was found that pitting potential shifted to more negative values and at the same time the value of current density increased at any give anodic potential, indicating the acceleration of pit initiation and growth.

In the same manner as Fig. 6, the values of D_f of pit morphology of alloy 600 in 0.5 M NaCl solution were determined at various solution temperatures. The resulting values of D_f of the pits are illustrated in Fig. 9 as a function of solution temperature. It was observed the value of D_f increased with increasing solution temperature. This means that the roughness of the corrosion pits formed at elevated solution temperature increases due to the acceleration of pitting corrosion.

3.2. Effect of anion additives

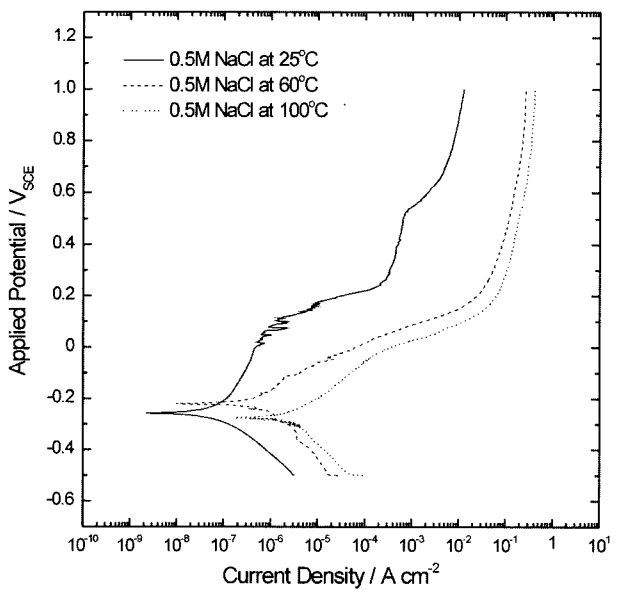

Fig. 8. Potentiodynamic polarization curves of alloy 600 with a scan rate of 0.5 mVs^{-1} in aqueous 0.5 M NaCl solution at various solution temperatures 25° to 100°C.

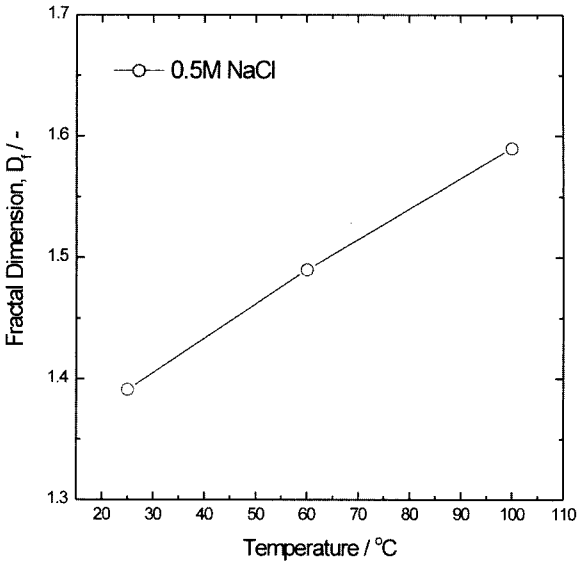

Fig. 9. Change in the value of the fractal dimension D_f determined by perimeter-area method for pit morphology on the surface of alloy 600 subjected to a constant anodic potential of 1.0 $V_{Ag/AgCl}$ in aqueous 0.5 M NaCl solution at various solution temperatures.

3.2.1. Effect of thiosulphate ($S_2O_3^{2-}$) ion

Figs. 10 (a) through (d) present SEM micrographs of the pits formed on alloy 600 in aqueous solution containing various concentrations of Cl^- and $S_2O_3^{2-}$ ions. From these figures, it is evident that $S_2O_3^{2-}$ ions play an important role in the process of pit growth. $S_2O_3^{2-}$ ions may react with nickel ions on the alloy surface, and hence the resulting nickel sulfide (Ni_3S_2) reduces the pH value of the solution in the pits. Thus, it accelerates the growth of the pits.

Figs. 11 (a) through (c) depict pit number density and average pit depth of the pits formed on alloy 600 after anodic polarization scans in Cl^- and $S_2O_3^{2-}$ solutions as a function of anion concentration. Pit number density and average pit depth increased with increasing Cl^- ion concentration. The corrosion potential at the pit bottom is very active due to the increased concentration of anions and the depletion of cations. On the other hand, the mouth of the pit, which serves as the cathode for the reduction of O_2, would attain a noble potential. Therefore, during pit growth, a potential distribution is established inside the pit.

In a solution with low Cl^- ion concentration, a large difference in ohmic resistance between the pit wall and the pit bottom could be expected due to the increased pit deposits as compared to a solution with high Cl^- ion concentration. This leads to a steeper potential gradient in the pit, subsequently, to a lower value of current density at the pit bottom, indicating shallower pit depth as given in Fig. 11(a) and (b).

When alloy 600 is immersed in chloride solution with 10^{-4} M $S_2O_3^{2-}$ ions addition, pit number density is larger than that in chloride solution without $S_2O_3^{2-}$ ions addition. In the case of 0.1 M chloride solution with $S_2O_3^{2-}$ ions addition, pit number density increased with decreasing $S_2O_3^{2-}$ ion concentration. This may be due to the fact that alloy 600 in low

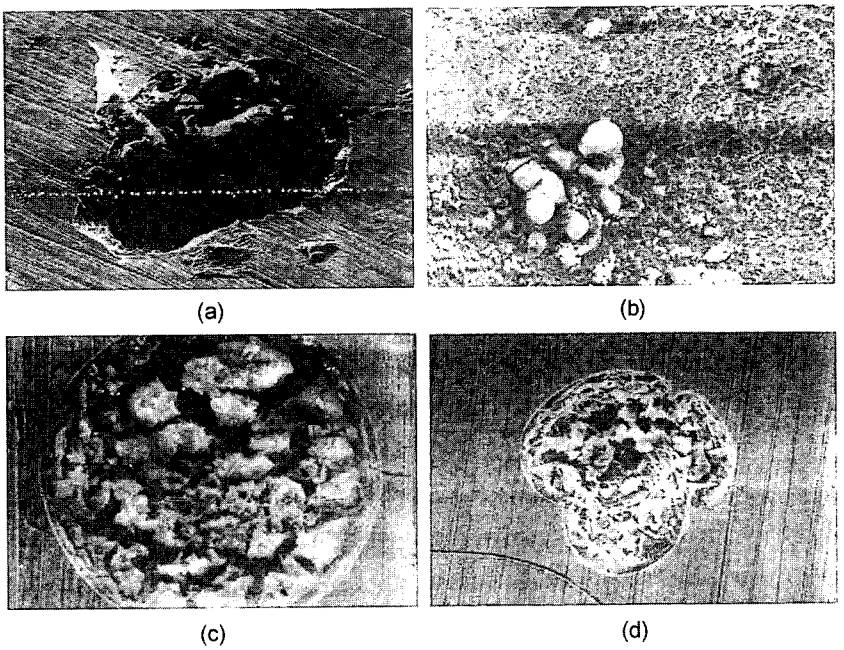

Fig. 10. SEM micrographs of the pits formed on alloy 600 in various concentrations of chloride (Cl^-) and thiosulfate ($S_2O_3^{2-}$) ions: (a) $[Cl^-] = 10^{-1}$ M, (b) $[Cl^-] = 10^{-1}$ M, $[S_2O_3^{2-}] = 10^{-1}$ M, (c) $[Cl^-] = 10^{-2}$ M, $[S_2O_3^{2-}] = 10^{-4}$ M, and (d) $[Cl^-] = 10^{-4}$ M, $[S_2O_3^{2-}] = 10^{-4}$ M[33].

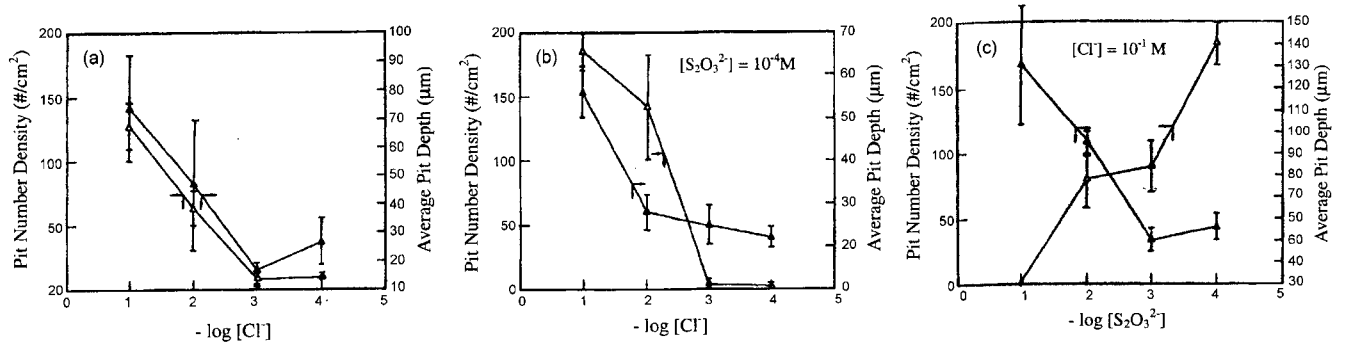

Fig. 11. Changes in pit number density and average pit depth of the pits formed on alloy 600 as functions of concentrations of chloride and thiosulfate ions[33].

$S_2O_3^{2-}$ ion concentration solution has more pit initiation sites compared with those in high $S_2O_3^{2-}$ ion concentration solution.

3.2.2. Effect of sulphate (SO_4^{2-}) ion with respect to solution temperature

Figs. 12(a) and (b) show typical SEM micrographs of pit morphology on the surface of alloy 600 subjected to a constant anodic potential of 1 $V_{Ag/AgCl}$ for 500s in aqueous 0.5 M NaCl solution containing various Na_2SO_4 concentrations of 0.01 and 0.05 M, respectively, at 25°C. It was observed that pit morphology became more simplified at the pit rim (boundary) with increasing SO_4^{2-} ion concentration. This means that the local attack at the pit rim was hindered by the addition of SO_4^{2-} ions to NaCl solution at room temperature due to the competitive adsorption of SO_4^{2-} ions with Cl^- ions.

Figs. 13 and 14 give typical SEM micrographs of pit morphology on the surface of alloy 600 subjected to a constant anodic potential of 1 $V_{Ag/AgCl}$ for 500s in aqueous 0.5 M NaCl solution containing various Na_2SO_4 concentrations at 60° and 100°C, respectively. In contrast to the case at room temperature, it was found that pit morphology became more complicated at the pit rim with increasing SO_4^{2-} ion concentration, indicating the acceleration of the local attack at the pit rim at elevated solution temperature.

This was experimentally verified by the analysis of potentiostatic current transients with respect to solution temperature. In the presence of SO_4^{2-} ions, it should be noted that SO_4^{2-} ions have two competing effects on the pitting process with respect to solution temperature. Fig. 15 shows potentiostatic current transients for alloy 600 subjected to a constant anodic potential of 1 $V_{Ag/AgCl}$ in aqueous 0.5 M NaCl solutions containing various Na_2SO_4 concentrations at various solution temperatures. At 25°C, it is easily seen from Fig. 15 (a) that the value of current density decreased with increasing SO_4^{2-} ion concentration over the whole time. This means that the addition of SO_4^{2-} ions impedes the whole pitting processes, *i.e.*, pit initiation and pit growth, at room temperature.

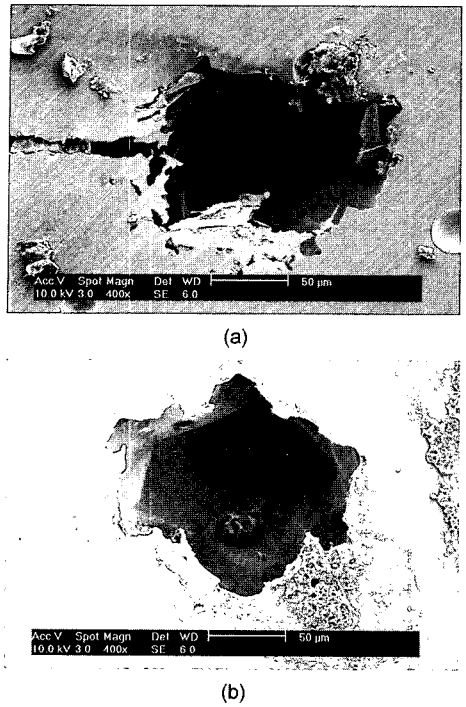

Fig. 12. SEM micrographs of pit morphology on the surface of alloy 600 subjected to a constant anodic potential of 1 $V_{Ag/AgCl}$ for 100 s in aqueous 0.5 M NaCl solutions containing various Na_2SO_4 concentrations of (a) 10^{-2} M and (b) 5×10^{-2} M at 25°C.

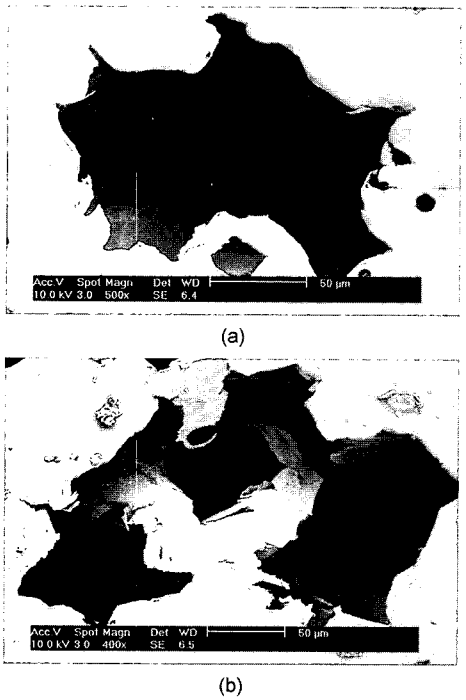

Fig. 13. SEM micrographs of pit morphology on the surface of alloy 600 subjected to a constant anodic potential of 1 $V_{Ag/AgCl}$ for 100 s in aqueous 0.5 M NaCl solutions containing various Na_2SO_4 concentrations of (a) 10^{-2} M and (b) 5×10^{-2} M at 60°C.

Above 60°C, it was found that the value of current density decreased with increasing SO_4^{2-} ion concentration in the current density-ascending region, indicating the inhibiting effect

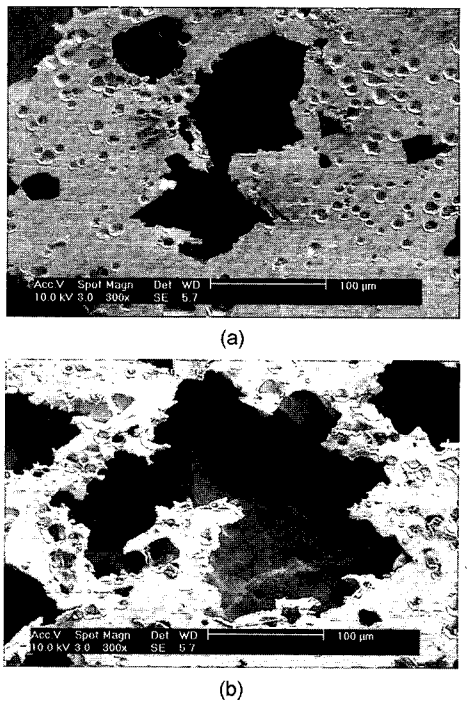

Fig. 14. SEM micrographs of pit morphology on the surface of alloy 600 subjected to a constant anodic potential of 1 $V_{Ag/AgCl}$ for 100 s in aqueous 0.5 M NaCl solutions containing various Na_2SO_4 concentrations of (a) 10^{-2} M and (b) 5×10^{-2} M at 100°C.

of SO_4^{2-} ions on the pit initiation. After that, that value of current density was found to increase with SO_4^{2-} ion concentration, implying the accelerating effect of SO_4^{2-} ions on the pit growth after pit initiation.

Now, it should be stressed that from the viewpoint of fractal geometry, such irregular morphologies of the pits as shown in Figs. 12 to 14 formed on the surface can be distinguishable from one another by means of D_f. The values of D_f of the pits determined by using perimeter-area method and the resulting values are summarized in Fig. 16 as functions of SO_4^{2-} ion concentration and solution temperature.

At 25°C, the value of D_f of the pits decreased with increasing SO_4^{2-} ion concentration. This means that the addition of SO_4^{2-} ions to NaCl solution hinders the local attack by Cl^- ions at the pit rim as a result of the competitive adsorption with Cl^- ions. Accordingly, weakened local attack at the pit rim causes the reduction in the value of pit perimeter and hence the value of D_f of the pits decreases with increasing SO_4^{2-} ion concentration at room temperature.

By contrast, above 60°C, the value of D_f of the pits rose with increasing SO_4^{2-} ions concentration. From this, it is readily inferred that the addition of SO_4^{2-} ions to NaCl solution enhances the local attack at elevated solution temperature.

Fig. 17 demonstrates changes in the value of the depression parameter determined from impedance spectra of alloy 600 as functions of SO_4^{2-} ion concentration and solution temperature. At room temperature, the value of the depression parameter increased with increasing SO_4^{2-} ion concentration, but that value of the depression parameter decreased with

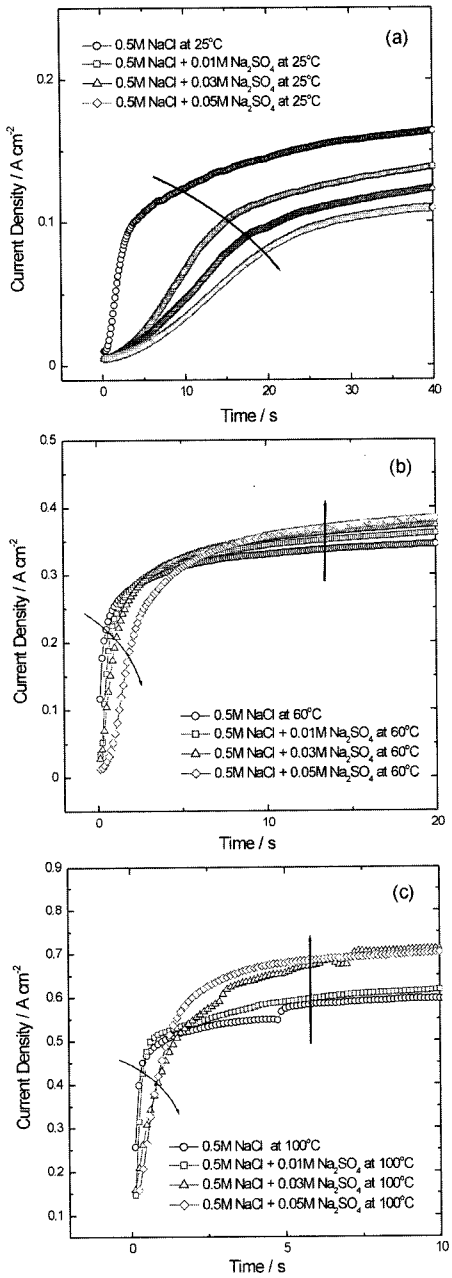

Fig. 15. Potentiostatic current transients for alloy 600 subjected to a constant anodic potential of 1 $V_{Ag/AgCl}$ in aqueous 0.5 M NaCl solutions containing various Na_2SO_4 concentrations at various solution temperatures of (a) 25°, (b) 60° and (c) 100°C.

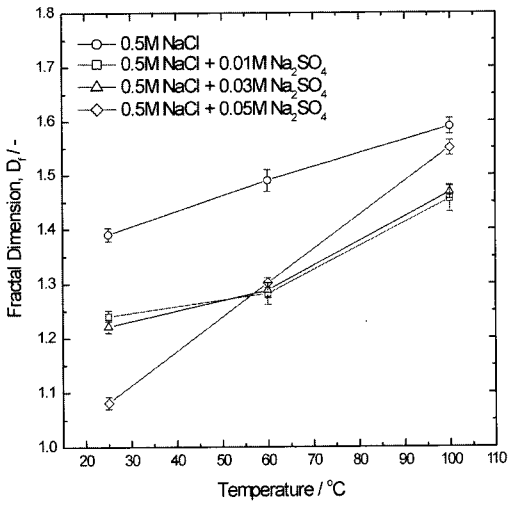

Fig. 16. Changes in the value of fractal dimension D_f determined by perimeter-area method for pit morphology on the surface of alloy 600 subjected to a constant anodic potential of 1.0 $V_{Ag/AgCl}$ for 100s in aqueous 0.5M NaCl solutions containing various concentrations of Na_2SO_4 at various solution temperatures.

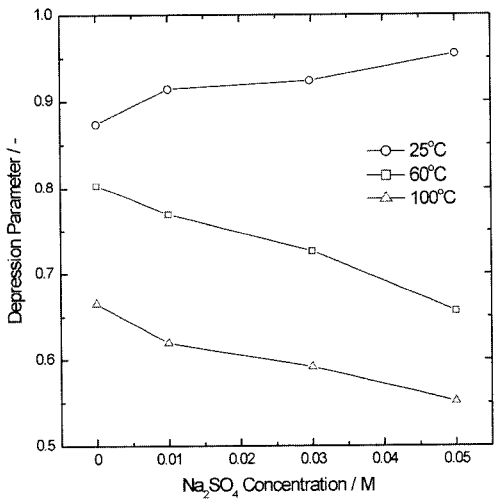

Fig. 17. Changes in the value of the depression parameter determined from impedance spectra of alloy 600 obtained at open circuit potential in aqueous 0.5 M Na_2SO_4 solution at room temperature after polarization of 1 $V_{Ag/AgCl}$ for 100 s in 0.5 M NaCl solutions containing various concentrations of Na_2SO_4 at various solution temperatures.

SO_4^{2-} ion concentration above 60°C. This involves that SO_4^{2-} ion addition makes the electrode surface more roughened due to the promotion of the pit growth at elevated solution temperature.

3.2.3. Effect of nitrate (NO_3^-) and bicarbonate (HCO_3^-) ions with respect to solution temperature

Fig. 18 gives changes in the value of fractal dimension D_f determined by perimeter-area method for pit morphology on the surface of alloy 600 in aqueous 0.5 M NaCl solutions containing various NO_3^- and HCO_3^- ions concentrations at various solution temperatures. In this figure, it is easily seen that the value of D_f of the pits decreased with increasing NO_3^- and HCO_3^- ions concentration, irrespective of solution temperature. From this, it is readily inferred that the addition of NO_3^- and HCO_3^- ions to NaCl solution prevents the local attack at the pit rim due to the competitive adsorption with Cl^- ions.

Fig. 19 demonstrates changes in the value of the depression parameter determined from impedance spectra of alloy 600 as functions of NO_3^- and HCO_3^- ions concentration and solution temperature. The value of the depression parameter decreased with increasing solution temperature for all kinds

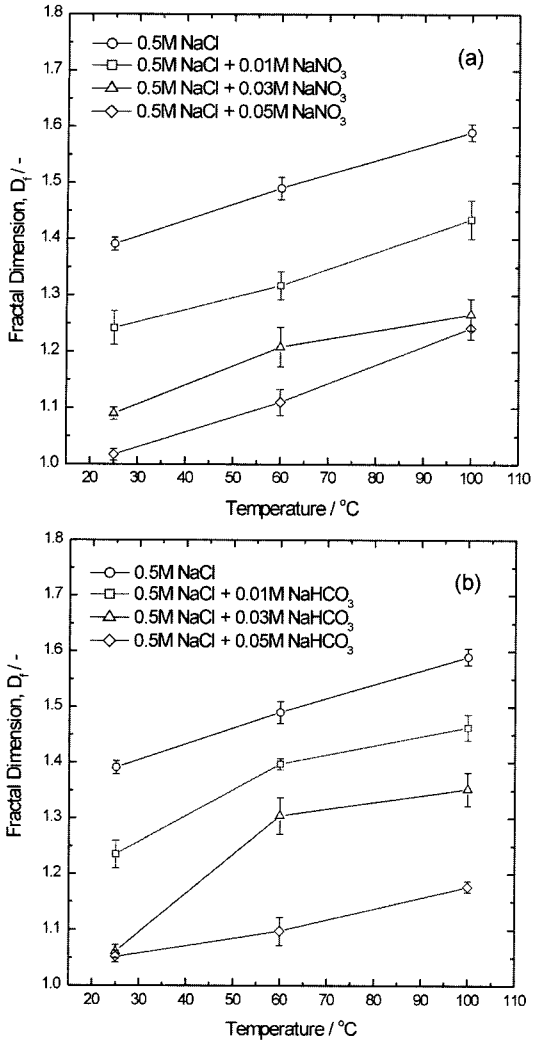

Fig. 18. Changes in the value of fractal dimension D_f determined by perimeter-area method for pit morphology on the surface of alloy 600 subjected to a constant anodic potential of 1.0 $V_{Ag/AgCl}$ for 100 s in aqueous 0.5 M NaCl solutions containing various concentrations of (a) $NaNO_3$ and (b) $NaHCO_3$ at various solution temperatures.

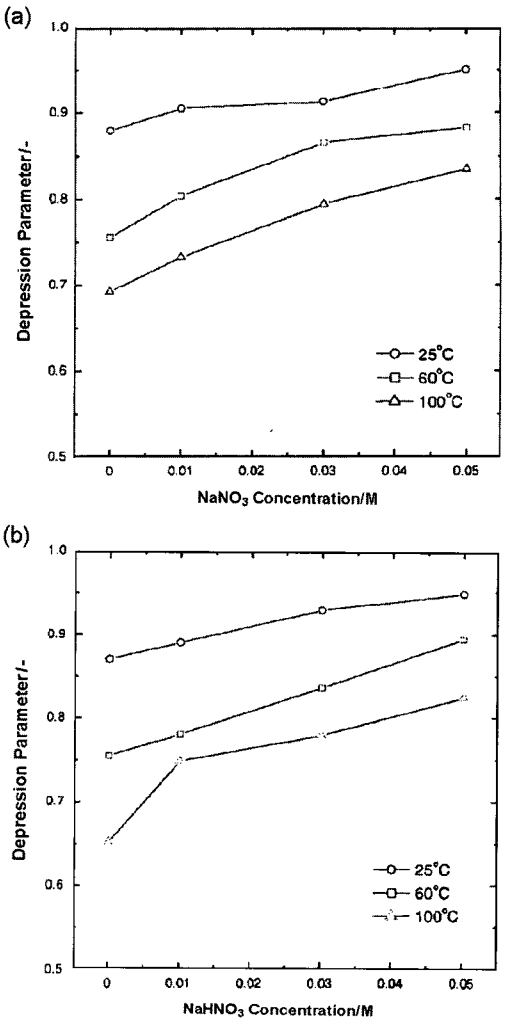

Fig. 19. Changes in the value of the depression parameter determined from impedance spectra of alloy 600 obtained at open circuit potential in aqueous 0.5 M Na_2SO_4 solution at room temperature after polarization of 1 $V_{Ag/AgCl}$ for 100 s in 0.5 M NaCl solutions containing various concentrations of (a) $NaNO_3$ and (b) $NaHCO_3$ at various solution temperatures.

of solutions. In addition, it was found that the value of the depression parameter increased with increasing NO_3^- and HCO_3^- ions concentration, irrespective of solution temperature. This implies that the addition of NO_3^- and HCO_3^- ions to NaCl solution reduces the roughness of the pits.

At this point, it is necessary to clarify the relationship between the D_f and the depression parameter. It should be emphasized that since the value of D_f determined by perimeter-area method represents the degree of the complexity of the two-dimensional pit morphology on the surface as a number, it can not give information about morphology of the inside of the pits. On the other hand, the depression parameter depicts the roughness of the pits, *i.e.*, the three-dimensional pit morphology.

It is generally agreed[49] that the value of D_f is inversely proportional to that value of the depression parameter. From the experimental findings of Figs. 16 to 19, it was noted that the value of the depression parameter shows a reverse tendency compared with that value of D_f for all kinds of solutions. From this, we can visualize the three-dimensional pit morphology including the inside of the pits in terms of the changes in the value of D_f. As a result, it is concluded that the inside of the pits shows the same tendency to change in morphology as compared with the two-dimensional pit morphology observed only on the electrode surface.

4. Conclusions

This article first summarized the previous works on the characteristics such as chemical composition, structure and passivity and on growth models of oxide film formed on alloy 600 at elevated solution temperatures. After that, this article reviewed previous works on the morphological change in the corrosion pits formed on alloy 600 as functions of

solution temperatures and such anion additives as thiosulphate, sulphate, nitrate and bicarbonate ions in terms of pit morphology and its fractal dimension.

From the value of the fractal dimension of pit morphology, it was found that solution temperature raised the value of the fractal dimension of the pits due to the increase in the roughness of the pits. In addition, in the presence of anion additives, it is realized that the addition of SO_4^{2-} ions to NaCl solution enhances the local attack at elevated solution temperature, whereas the addition of NO_3^- and HCO_3^- ions to NaCl solution prevents the local attack, irrespective of solution temperature.

From the experimental findings, it is inferred that the fractal dimension of the corrosion pits maintains nearly constant in value during the whole pitting process at each solution temperature, irrespective of pit size, suggesting unchangeable pit morphology during pit growth. In addition, from the fact that the value of the depression parameter is inversely proportional to that value of the fractal dimension, it is concluded that the three-dimensional pit morphology including the inside of the pits can be described by the change in the value of the fractal dimension.

Acknowledgements

This work was partly supported by the Brain Korea 21 project.

References

1. J. Hickling and B. Wieling, *Corrosion*, **37**, 1475 (1981).
2. P. J. King and D. P. Doutovich, *Nuclear Tech.*, **55**, 196 (1981).
3. J. R. Park and Z. Szkalarska-Smialowska, *Corrosion*, **41**, 665 (1985).
4. D. Choi and G. S. Was, *Corrosion*, **48**, 292 (1992).
5. M. Y. Chang and G. P. Yu, *J. Nuc. Mat.*, **202**, 145 (1993).
6. C. J. Semino, P. Pedeferri, G. T. Burstein and T. P. Hoar, *Corros. Sci.*, **19**, 1069 (1979).
7. J. Hickling and N. Wieling, *Corrosion*, **37**, 147 (1981).
8. Z. Szklarska-Smialowska, *Corros. Sci.*, **18**, 97 (1978).
9. G. Palumbo, P. J. King and K. T. Aust, *Corrosion*, **43**, 37 (1987).
10. H. Bohni and H. H. Uhlig, *J. Electrochem. Soc.*, **116**, 906 (1969).
11. M. E. Curley-Fiorino and G. M. Schmid, *Corros. Sci.*, **20**, 313 (1980).
12. D. H. Lister, *Nucl. Sci. and Eng.*, **58**, 239 (1975).
13. D. H. Lister, *Nucl. Sci. and Eng.*, **59**, 406 (1976).
14. R. L. Tapping, R. D. Davidson, E. McAlpine and D. H. Lister, *Corros. Sci.*, **26**, 563 (1986).
15. D. H. Lister, R. D. Davidson and E. McAlpine, *Corros. Sci.*, **27**, 113 (1987).
16. M. E. Pick and M. G. Segal, *Nucl. Eng.*, 22, 433 (1983).
17. R. Bauch, M. Cambini, P. Weisgerber, C. De Asmundis and C. Plog, *J. Nucl. Mater.*, **92**, 334 (1980).
18. M. G. Alvarez, A. M. Olmedo and M. Villegas, *J. Nuclear Materials*, **229**, 93 (1996).
19. Y. Asakura, H. Karasawa, M. Sakagami and S. Uchida, *Corrosion*, **45**, 119 (1989).
20. I. Michel and C. Plog, *Metall*, **31**, 252 (1977).
21. M. Warzee, C. Sonnen and Ph. Berge, "Corrosion of Carbon Steels and Stainless Steels in Pressurized Water of High Temperatures", European Atomic Energy Commission, Report, July (1967).
22. J. H. Wang, C. C. Su and Z. Szklarska-Smialowska, *Corrosion*, **44**, 732 (1988).
23. J. Robertson, *Corros. Sci.*, **29**, 1275 (1989).
24. B. Stellwag, *Corrosion*, **53**, 120 (1997).
25. A. Gebert, F. Schneider and K. Mummert, *Nuclear Engineering and Design*, **174**, 327 (1997).
26. J. Robertson, In Proc. Conf. Water Chemistry of Nucl. Reactor Systems, **5**, Bournemouth, Oct. (1989), British Nuclear Engineering Society, London, **1**, 81 (1989).
27. F. Michel and R. Winkler, *Werkstoffe und Korrosion*, **39**, 412 (1988).
28. J.-J. Park, S.-I. Pyun and S.-B. Lee, *Electrochim. Acta*, press in (2003)
29. C. Y. Chao, L. F. Lin and D. D. Macdonald, *J. Electrochem. Soc.* **128**, 1187 (1981).
30. D. D. Macdonald, S. R. Biaggio and H. Song, *J. Electrochem. Soc.* **139**, 170 (1992).
31. D. D. Macdonald, *J. Electrochem. Soc.* **139**, 3434 (1992).
32. S.-I. Pyun and M.-H. Hong, *Electrochim. Acta*, **37**, 327 (1992).
33. J. T. Ho and G. P. Yu, *Corrosion*, **48**, 147(1992).
34. J.-J. Park and S.-I. Pyun, *Corros. Sci.*, **45**, 995 (2003).
35. J.-J. Park and S.-I. Pyun, *J. Solid State Electrochem.* **7**, 380 (2003).
36. S.-I. Pyun and J.-J. Park, *J. Solid State Electrochem.*, press in (2003).
37. W. F. Bogaerts, A. A. Van Haute and M. J. Brabers, *J. Nucl. Mater.*, **115**, 339 (1983).
38. Z. Szklarska-Smialowska, D. Grimes and J. Park, *Corros. Sci.*, **27**, 859 (1987).
39. N. Sato, *Corros. Sci.*, **37**, 1947 (1995).
40. A. M. Olmedo, M. Villegas and M. G. Alvarez, *J. Nuclear Materials*, **229**, 102 (1996).
41. H.-C. Shin and J.-Y. Go, private communication, KAIST, Daejeon, Republic of Korea (2001).
42. B. B. Mandelbrot, D. E. Passoja and A. J. Paullay, *Nature*, **308**, 721 (1984).
43. B. B. Mandelbrot, *Physica Scripta*, **32**, 257 (1985).
44. J. Feder, "Fractals", Plenum, New York, p.200 (1988).
45. J. M. Gómez-Rodriguez, A. M. Baró, L. Vázquex, R. C. Salvarezza, J. M. Vara and A. J. Ariva, *J. Phys. Chem.*, **96**, 347 (1992).
46. P. Herrasti, P. Ocón, R. C. Salvarezza, J. M. Vara, L. Vázquez and A. J. Arvia, *Electrochim. Acta*, **37**, 2209 (1992).
47. P. L. Antonucci, R. Barberi, A. S. Aricò, A. Amoddeo and V. Antonucci, *Mat. Sci. & Eng. B*, **38**, 9 (1996).
48. T. Silk, Q. Hong, J. Tamm and R. C. Compton, *Synth. Metals*, **93**, 65 (1998).
49. U. Rammelt and G. Reinhard, *Corros. Sci.*, **27**, 373 (1987).
50. W. H. Mulder and J. H. Sluyters, *Electrochim. Acta*, **33**, 303 (1988).
51. T. Pajkossy, *J. Electroanal. Chem.*, **364**, 111 (1994).